Photometric modeling and VIS-IR albedo maps of Dione from Cassini-VIMS

G. Filacchione[1], M. Ciarniello[1], E. D'Aversa[1], F. Capaccioni[1], P. Cerroni[1], B. Buratti[2], R. N. Clark[3], K. Stephan[4], C. Plainaki[5]

[1]INAF-IAPS, Istituto di Astrofisica e Planetologia Spaziali, Rome, Italy.
[2]Jet Propulsion Laboratory, California Institute of Technology, Pasadena, CA, USA.
[3]PSI Planetary Science Institute, Tucson, AZ, USA.
[4]DLR, German Aerospace Center, Berlin, Germany.
[5]ASI, Italian Space Agency, Rome, Italy

Key Points:

- Application of photometric correction to Cassini-VIMS data.
- Computation of Dione albedo maps at VIS and IR wavelengths.
- Retrieval of VIS slopes and water ice band depth maps.

Corresponding author: G. Filacchione, gianrico.filacchione@iaps.inaf.it

Abstract

We report about visible and infrared albedo maps and spectral indicators of Dione's surface derived from the complete VIMS dataset acquired between 2004 and 2017 during the Cassini tour in the Saturn's system. Maps are derived by applying a photometric correction necessary to disentangle the intrinsic albedo of the surface from illumination and viewing geometry occurring at the time of the observation. The photometric correction is based on the *Shkuratov et al.* [2011] method which yelds values of the surface equigonal albedo. Dione's surface albedo maps are rendered at five visible (0.35, 0.44, 0.55, 0.7, 0.95 μm) and five infrared (1.046, 1.540, 1.822, 2.050, 2.200 μm) wavelengths in cylindrical projection with a $0.5° \times 0.5°$ angular resolution in latitude and longitude, corresponding to a spatial resolution of 4.5 km/bin. Apart from visible and infrared albedo maps, we report about the distribution of the two visible spectral slopes (0.35-0.55 and 0.55-0.95 μm) and water ice 2.050 μm band depth computed after having applied the photometric correction. The derived spectral indicators are employed to trace Dione's composition variability on both global and local scales allowing to study the dichotomy between the bright-leading and dark-trailing hemispheres, the distribution of fresh material on the impact craters and surrounding ejecta and the resurfacing of the bright material within the chasmata caused by tectonism.

1 Introduction

The application of a photometric correction to icy surfaces hyperspectral data is an operation necessary to remove the illumination and viewing effects from I/F spectra, to derive spectral reflectance and to correctly associate spectral variations to changes in composition or physical properties of the surface. Different models have been proposed to model the phase function of a planetary surface by using parameters that depend on the physical characteristics of the regolith, such as the surface's scattering behavior, roughness and porosity. The most widely used models are those based on *Minnaert* [1941], *Hapke* [1993, 2002] and *Shkuratov et al.* [1999] formulations. Other authors have modeled the surface phase function by fitting the observational data with polynomial series [*Hillier et al.*, 1999; *Buratti et al.*, 2011; *Hicks et al.*, 2011; *Besse et al.*, 2013].

In this work we are adopting the *Shkuratov et al.* [2011] photometric correction to derive albedo maps of Dione's surface from disk-resolved Cassini VIMS data spanning in the 0.35-5.0 μm spectral range. VIMS data have already been exploited to realize global compositional maps of Dione following different approaches to mitigate the effects of the photometric response of the surface: *Stephan et al.* [2010] and *Scipioni et al.* [2013] have used the Spectral Angle Mapper [*Yuhas et al.*, 1992] to compare the surface spectral properties with previously-defined spectral endmembers. This technique reduces the influence of the photometric effects between pixels acquired at varying illumination/viewing geometries. Both authors have found a significant dichotomy between the bright water-ice rich leading hemisphere and the dark non-icy material on the trailing hemisphere. Moreover, they have found that bright and water ice-rich units are those associated with the ejecta departing from the geologically recent Creusa crater and with the linear features probably caused by tectonism. In *Scipioni et al.* [2017] several spectral indicators have been used to trace the distribution of the submicron grains caused by the bombardment of charged particles and by micrometeorite gardening. The resulting maps were built without applying an exhaustive photometric correction but only normalizing VIMS data at a fixed wavelength (2.230 μm). The analysis performed by *Clark et al.* [2008] indicates that the dark material on the trailing hemisphere of Dione is caused by the bombardment of dark submicron grains originated outside the Saturnian system, possibly of cometary or Kuiper Belt origin. These submicron particles are also the scatterers originating the Rayleigh scattering visible in the blue spectral range . All these results were achieved from a VIMS mosaic acquired during the 2005 October 11th flyby with a fixed phase angle of 22°. A

comparison of Dione disk-integrated colors and water ice band properties retrieved from observations taken in a wide range of illumination and viewing geometries in the context of the other Saturn's system satellites and rings is given in *Filacchione et al.* [2012, 2013]. So far, the best spatially-resolved albedo map of Dione has been derived from ISS camera images by *Schenk et al.* [2011]. The map is photometrically-corrected at visible colors reaching a spatial resolution of 1-1.5 km/pixel above the entire surface of the satellite. The add-on of this work is the exploitation of the complete VIMS dataset and the application of a rigorous formalism to derive photometric correction necessary to compute visible - near infrared albedo and spectral indicators maps of Dione.

2 Observations and data selection

During the 13 years-long Cassini mission in the Saturn's system, VIMS the Visual and Infrared Mapping Spectrometer [*Brown et al.*, 2004], has collected hyperspectral data of Dione's surface during five targeted flybys occurred on 2005 October 11th, closest approach at 17:59 at a minimum distance of 500 Km; 2010 April 7th, 05:16, 503 Km; 2011 December 12th, 09:39, 99 Km; 2015 June 16th, 20:12, 516 Km; 2015 August 17th, 18:33, 474 Km. Apart from the aforementioned cases, VIMS has returned disk-resolved data on numerous other occasions from greater distances, extending the spatial coverage at lower resolution and at varying illumination/viewing conditions. This dataset has been used to perform disk-integrated observation analysis [*Filacchione et al.*, 2007, 2010]. In this work we have exploited the entire VIMS dataset by searching all observations targeted at Dione. VIMS data have been calibrated in radiance factor units, I/F (where I is the reflected intensity of light from the surface and πF is the plane-parallel incident solar flux) using the RC17 version pipeline [*Clark et al.*, 2012]. Each VIMS observation geometry has been computed by means of SPICE reconstructed kernels [*Acton*, 1996] which determine the geographic position of each VIMS pixel on Dione's surface (longitude, latitude position), the corresponding illumination and viewing conditions (incidence, emission, phase angles, local solar time) and spatial resolution (Cassini altitude above the surface). These quantities are computed at the pixel's center and on the 4 corners of the pixel for the entire Dione dataset. A total of 421,323 and 470,490 pixels are acquired on Dione's surface from the VIMS-VIS and IR spectral channels, respectively. However, not all these datapoints are useful for building an albedo map because unfavourable observation geometry sometimes occurs resulting in poor spatial resolution or in too much oblique illumination and viewing angles. In addition, the signal in some low phase observations is saturated and unusable. The dataset is therefore filtered to reduce the presence of shadows caused by topography, to achieve a good signal to noise and to remove extreme observation conditions not suitable for the production of global maps. As a consequence of these requirements, the following rules have been applied to the dataset to exploit only the good pixels: 1) unsaturated signal lower than 4,000 DN[1]; 2) values of the incidence and emission angles on the pixel's center $\leq$ 80°; 3) value of the solar phase angle on the pixel's center $10° \leq phase \leq 90°$; 4) Cassini altitude $\leq$ 100,000 km from the surface, corresponding to a spatial resolution better than 50 km/px in nominal resolution mode and 17 or 17×25 km in high resolution mode respectively for the VIS and IR channels. By applying these criteria the filtered dataset is reduced to 156,728 and 167,787 pixels respectively for the VIS (at 0.55 μm) and IR (at 1.046 μm) channels. The photometric correction and resulting albedo maps shown later are derived by processing the filtered datasets.

3 Photometric Correction

In this work we have adopted the method given by *Shkuratov et al.* [2011] to photometrically correct the Cassini VIMS data of Dione. A similar approach has been success-

[1] VIMS detectors have a dynamical range of 12 bits, corresponding to 1-4096 DN

fully applied to other solar system bodies, e.g. Mercury [*Domingue et al.*, 2016], asteroids 4 Vesta and 21 Lutetia [*Longobardo et al.*, 2016] and the Earth's Moon [*Kaidash et al.*, 2009].

For a given geometry defined by means of incidence (i), emission (e) and phase (g) angles, the radiance factor $I/F(\lambda,i,e,g)$ is given by the product:

$$\frac{I}{F}(\lambda,i,e,g) = D(i,e,g) \times F(\lambda,g) \tag{1}$$

where D(i,e,g) is the disk function and F(λ, g) is the phase function which includes the albedo. The disk function D is computed following the Akimov model [*Shkuratov et al.*, 1999]:

$$D(i,e,g) = D(\beta,\gamma,g) = \cos\left(\frac{g}{2}\right)\cos\left[\frac{\pi}{\pi-g}\left(\gamma-\frac{g}{2}\right)\right]\frac{(\cos\beta)^{\frac{g}{\pi-g}}}{\cos\gamma} \tag{2}$$

where γ, β are the photometric longitude and latitude, respectively, defined as:

$$\gamma = arctan\left(\frac{cos(i)-cos(e)cos(g)}{cos(e)sin(g)}\right) \tag{3}$$

$$\beta = arccos\left(\frac{cos(e)}{cos(\gamma)}\right) \tag{4}$$

The phase function $F(\lambda,g)$ can be derived by applying an arbitrary fit to the observation data corrected for the disk function D. In our case we have used a 2-nd degree polynomial fit. From eq. 1 we derive:

$$\frac{\frac{I}{F}(\lambda)}{D} = a + bg + cg^2 \tag{5}$$

which at null phase gives the value of the equigonal albedo a:

$$\frac{I}{F}(\lambda,g=0) = a \tag{6}$$

being D(g=0)=1. In this work, the equigonal albedo a corresponds to the albedo at g=0° as derived from the polynomial fit applied to observations taken at phase angles not affected by the opposition surge. The phase angle range in the Dione dataset is $10° \leq g \leq 120°$. For this reason, since the equigonal albedo does not model the opposition effect surge, it is lower than the normal albedo as defined in *Hapke* [1993]. When comparing the results of this work with others in literature is necessary to consider this difference.

4 Phase curve fitting and photometry parameters derivation

The photometric fit parameters a,b,c in eq. 5 are computed on the distribution of the (I/F)/D for the filtered pixels as a function of the phase g. As an example, in Figure 1 the best fit to the data at 0.55 μm is shown. VIMS data are not filtered for specific terrains units (bright or dark areas) and therefore show an intrinsic variability along the vertical axis. Since we aim to derive parameters able to photometrically correct the average terrain, we need to manage this spread to achieve the best-fit solution. The fit is performed in two steps to reduce the effects caused by the clutter of the observations. As a first step the polynomial fit (blue curve) is computed on the entire dataset (black and orange points), including the pixels having a large spread caused by: 1) partially filled pixels occurring along limb and terminator; 2) mismatch between images and geometry

parameters as a consequence of inconsistencies in VIMS timing and/or accuracy of the reconstructed kernels. A second polynomial fit (red curve) is computed on a reduced dataset consisting of the points dispersed within -20% and +40% with respect the first fit (orange points). The parameters a, b, c computed on the second fit for the ten wavelengths analyzed in this work are listed in Table 1.

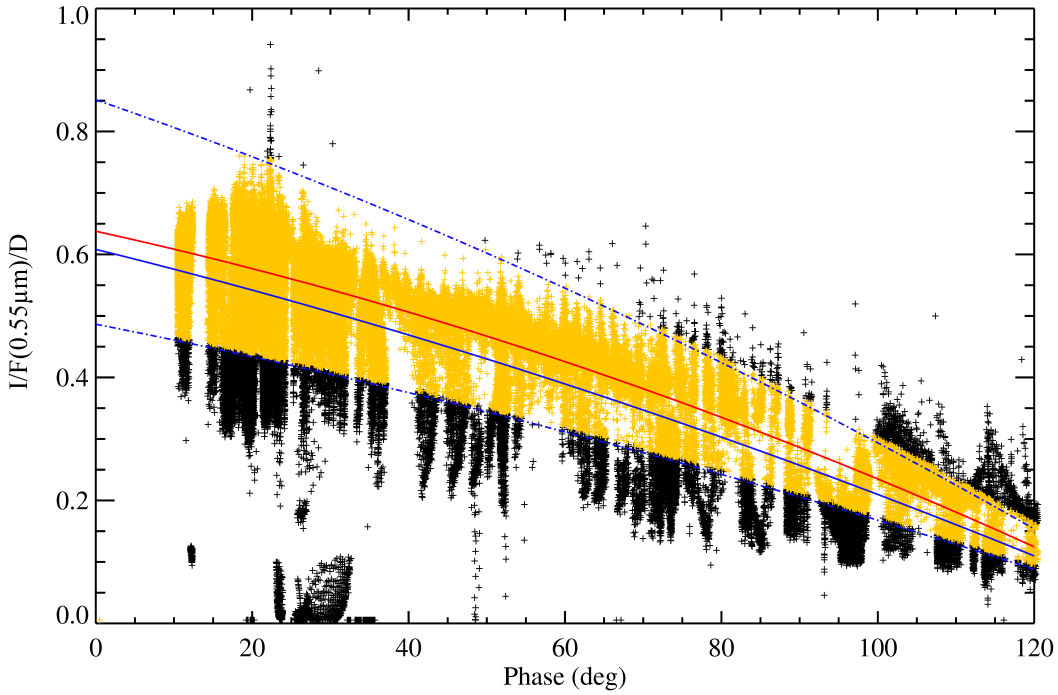

Figure 1. Dione's phase curve at 0.55 μm. The blue curve corresponds to the quadratic fit computed on all observations (black points). Orange points correspond to the subset of observations within -20% and +40% (blue dashed curves) of the first fit (blue curve) and are used to compute the second fit (red curve). The equigonal albedo of 0.62 is given by the red curve value at g=0.

5 Albedo maps

Albedo maps are built by applying the same mapping method discussed in *Filacchione et al.* [2016a,b] and *Ciarniello et al.* [2016]. While broad filtering conditions are used for the retrieval of the photometric parameters a, b, c, the selection of the data to build albedo maps has been truncated to incidence and emission angles $(i, e) \leq 50°$ and phase $10° \leq g \leq 70°$ in order to achieve better rendering results. The pixels simultaneously matching all these filtering conditions are projected on a cylindrical map by filling the area of the grid defined by the coordinates of the four corners. In case of multiple acquisitions above the same bin, the mean value of the albedo is computed and shown in the map. The cylindrical map has a spatial resolution of 0.5° × 0.5°/bin along longitude and latitude axes. With this sampling a resolution of 4.5 km/bin is reached at the equator. The average incidence, emission, phase angles and data redundancy (number of times a given bin has been observed) on the map are shown in Fig. 2 panels A)-D).

The photometrically-corrected equigonal albedo map at three visible colors (B=0.44 μm, G=0.55 μm and R=0.7 μm) is shown in Fig. 2 - panel E). The resulting data cov-

Table 1. Photometric fit parameters for the visible and infrared channels used to render albedo maps shown in Fig. 2-3 and spectral indicators in Fig. 4. The parameter *a* is the equigonal albedo value.

Wavelength (μm)	a	b	c
0.35	0.57582±0.00034	$-3.8629\cdot10^{-3}\pm1.79\cdot10^{-5}$	$-2.2568\cdot10^{-5}\pm1.72\cdot10^{-7}$
0.44	0.61407±0.00040	$-2.7793\cdot10^{-3}\pm2.10\cdot10^{-5}$	$-1.2833\cdot10^{-5}\pm1.98\cdot10^{-7}$
0.55	0.61977±0.00047	$-2.0784\cdot10^{-3}\pm2.44\cdot10^{-5}$	$-1.6930\cdot10^{-5}\pm2.27\cdot10^{-7}$
0.70	0.58411±0.00051	$-1.3168\cdot10^{-3}\pm2.63\cdot10^{-5}$	$-2.1872\cdot10^{-5}\pm2.43\cdot10^{-7}$
0.95	0.58268±0.00046	$-1.1177\cdot10^{-3}\pm2.39\cdot10^{-5}$	$-2.3364\cdot10^{-5}\pm2.24\cdot10^{-7}$
1.046	0.55834±0.00071	$-2.2498\cdot10^{-3}\pm3.81\cdot10^{-5}$	$-1.1178\cdot10^{-5}\pm3.83\cdot10^{-7}$
1.540	0.40562±0.00044	$-1.8476\cdot10^{-3}\pm2.34\cdot10^{-5}$	$-7.7896\cdot10^{-5}\pm2.30\cdot10^{-7}$
1.822	0.55832±0.00077	$0.4313\cdot10^{-3}\pm4.02\cdot10^{-5}$	$-3.7100\cdot10^{-5}\pm4.03\cdot10^{-7}$
2.050	0.24751±0.00023	$-1.6671\cdot10^{-3}\pm1.26\cdot10^{-5}$	$1.3615\cdot10^{-5}\pm1.22\cdot10^{-7}$
2.200	0.51508±0.00067	$0.1546\cdot10^{-3}\pm3.48\cdot10^{-5}$	$-3.0367\cdot10^{-5}\pm3.46\cdot10^{-7}$

erage spreads across the equatorial regions up to about latitude ±45° due to the limiting filtering conditions applied on the incidence and emission angles. Across the antisaturnian hemisphere (centered at longitude 180°) and leading hemisphere (centered at longitude 0°) the best coverage and data redundancy is reached. Conversely, wide gaps in coverage occur on the regions around longitude 90° and 270°. On the antisaturnian hemisphere the transition between the bright leading and the more dark trailing hemisphere is visible: several craters and chasmata are recognizable, as indicated by the numerals shown in Fig. 2 - panel E). Within the limits imposed by the wide excursion of the illumination and viewing conditions, the photometric correction is able to return quite homogenous and seamless albedo results. The major discrepancies are seen where redundancy is low, like on the edge starting from equator at lon=60° up to lon=45°, lat=45°, or where the incidence angle is changing rapidly, like around lon=135-180°, lat=-30° (Fig. 2 - panel A). For a comparison with ISS derived albedo maps at 1-1.5 km/bin resolution at visible colors (IR, Green, UV filters) the interested reader can refer to the work of *Schenk et al.* [2011] where a simplified lunar-lambertian photometric function [*McEwen*, 1991] has been applied. The spatial distribution of the visible albedo appears well-correlated with similar VIMS daytime temperature maps derived from the spectral properties of the 3.6 μm reflectance peak [*Filacchione et al.*, 2016a]: a maximum temperature of 140 K is measured above the equatorial dark units on the trailing hemisphere, about 30 K higher than on the bright water ice-rich areas on the leading equatorial regions.

The same methodology used to map visible images is applied to infrared data too. The albedo maps derived at 1.046, 1.540 and 2.200 μm are shown in Fig. 3. In this case we keep the three monochromatic maps separated because the spatial coverage among them is different and it is not feasible to retrieve a spatially homogeneous RGB combination like for the visible channel. We have selected these bands to check the capabilities of the photometric correction to derive satisfactory albedo maps on both high (1.046, 2.200 μm) and low (1.540 μm) reflectance bands. In the latter case there is a larger occurrence of unsaturated pixels with respect to the former ones. As a consequence of this effect, the 1.540 μm map has a wider spatial coverage across the dark wispy terrains on the trailing hemisphere (Fig. 3 - panel B). Apart from the coverage differences, the contrast among the three monochromatic maps appears different: on the water ice band at 1.540 μm the albedo variations are limited to the 0.32-0.42 range while on the continuum the albedo appears more variable in the range 0.43-0.61 and 0.39-0.55 for the 1.046 and 2.200 μm maps, respectively. Apart from the lower values measured across the wispy terrains units, no significant changes are seen in correspondence with the impact craters on the monochromatic maps shown in Fig. 3. The single color albedo maps are affected by

an average error between 2 and 3%. The maximum error is equal to 10% for bins affected by low data redundancy and poor illumination conditions.

6 Spectral indicators maps

After having applied the photometric correction it is possible to derive the spatial distribution of spectral indicators unaffected by illumination and viewing conditions. In this work we have derived three indicators, e.g. 0.35-0.55 μm spectral slope; 0.55-0.95 μm spectral slope; 2.05 μm water ice band depth. These indicators have been widely used in the past for the retrieval of surface compositions of the icy satellites [*Clark et al.*, 2008; *Stephan et al.*, 2010; *Filacchione et al.*, 2012; *Scipioni et al.*, 2013; *Filacchione et al.*, 2013]. The spectral slopes are computed from equigonal albedos at 0.35-0.55 μm and 0.55-0.95 μm. The band depth at 2.05 μm is computed with respect to the continuum estimated at 1.822 and 2.2 μm. The spectral indicator maps shown in Fig. 4 have been generated adopting the same method previously described for the equigonal albedo maps. The spectral slopes and water ice band depth are affected by error bars lower than 1% and 5%, respectively. The 0.35-0.55 μm slope map (panel A) shows a dicothomy between the leading and trailing hemispheres with a spatial distribution similar to the VIS albedo shown in Fig. 2 - panel E). The highest reddening is measured across the leading-antisaturnian quadrant ($90° \leq lon \leq 180°$) where the maximum slope of 0.6 μm^{-1} is reached on the Aeneas crater and on the Creusa crater ejecta (respectively indicated by labels 6 and 4 in Fig. 2). A local increase of the slope is observed also on the Sagaris crater (label 5). The reddening gradually reduces to 0.3 μm^{-1} moving towards the trailing hemisphere where it reaches neutral values on the dark terrain regions. While the 0.35-0.55 μm slope is positive (or red), the 0.55-0.95 μm slope map (panel B) has a negative (or blue) distribution with the lower value of -0.180 μm^{-1} across the antisaturnian hemisphere (around lon=180°) and on saturnian at lon=0°. The slope becomes more neutral in vicinity of the wispy terrains on the trailing side. The water ice 2.05 μm band depth map (panel C) shows a substantial difference between the two hemispheres: on the leading one the absorption is higher, reaching a maximum of 0.59 above the Aeneas crater and on the Creusa crater ejecta, the same areas where the 0.35-0.55 μm slope is maximum. On the dark units of the trailing hemisphere the band depth decreases reaching values as low as 0.34. These units have an exogenic origin resulting from the effect of charged particles and submicron grains bombardment [*Clark et al.*, 2008]. Above the bright streaks of Padua Chasmata (label 7) and Eurotas Chasmata (label 8) the band depth is ≥0.46, higher than on the surrounding dark terrains. These changes in band depth distribution are caused by tectonism which causes the resurfacing of bright ices within the chasmata features [*Stephan et al.*, 2010].

7 Conclusions

The average photometric response of Dione surface at five visible and five infrared wavelengths has been derived from the full VIMS dataset acquired during the entire Cassini mission at Saturn (from 2004 to 2017). The photometric correction disentangles the effects caused by the illumination and viewing geometry from surface properties and it yields values of equigonal albedo and spectral indicators (slopes, band depth). We underline that such a result has an inter-disciplinary impact since a more detailed knowledge of the surface's spectral properties can provide constraints for its erosion rate and evolution history. After having reported here about the methodology applied to the Dione dataset, we aim to build similar maps for the remaining Saturn's icy satellites at multiple wavelengths with the scope to determine the spatial distribution of the spectral indicators (spectral slopes, water ice band properties) from photometric-corrected data and to correlate them with morphological features of the surfaces. This will be the argument of a future paper.

Acknowledgments
The authors acknowledge the financial support from Italian Space Agency (ASI) for the Cassini-VIMS data analysis program. This research has made use of NASA's Astrophysics Data System.

References

Acton, C. (1996). Ancillary data services of NASA's Navigation and Ancillary Information Facility. *Planetary and Space Science*, 44, 65-70.

Besse, S., Sunshine, J., Staid, M., Boardman, J., Pieters, C., Guasqui, P., Malaret, E., McLaughlin, S., Yokota, Y., Li, J.-Y. (2013). A visible and near-infrared photometric correction for Moon Mineralogy Mapper (M^3). *Icarus*, 222, 229-242.

Brown, R. H., Baines, K. H., Bellucci, G., Bibring, J.-P., Buratti, B. J., Capaccioni, F., Cerroni, P., Clark, R. N., Coradini, A., Cruikshank, D. P., Drossart, P., Formisano, V., Jaumann, R., Langevin, Y., Matson, D. L., McCord, T. B., Mennella, V., Miller, E., Nelson, R. M., Nicholson, P. D., Sicardy, B., Sotin, C. (2004). The Cassini Visual And Infrared Mapping Spectrometer (Vims) Investigation. *Space Science Reviews*, 115, 111-168.

Buratti, B. J., Hicks, M. D., Nettles, J., Staid, M., Pieters, C. M., Sunshine, J., Boardman, J., Stone, T. C. (2011). A wavelength-dependent visible and infrared spectrophotometric function for the Moon based on ROLO data {textitJ. Geophys. Res. (Planets), 116, 8.

Ciarniello, M., Raponi, A., Capaccioni, F., Filacchione, G., Tosi, F., De Sanctis, M. C., Kappel, D., Rousseau, B., Arnold, G., Capria, M. T., Barucci, M. A., Quirico, E., Longobardo, A., Kuehrt, E., Mottola, S., Erard, S., Bockelée-Morvan, D., Leyrat, C., Migliorini, A., Zinzi, A., Palomba, E., Schmitt, B., Piccioni, G., Cerroni, P., Ip, W.-H., Rinaldi, G., Salatti, M. (2016). The global surface composition of 67P/Churyumov-Gerasimenko nucleus by Rosetta/VIRTIS. II) Diurnal and seasonal variability, *Monthly Notices of the Royal Astronomical Society*, 462, S443-S458.

Clark, R. N., Curchin, J. M., Jaumann, R., Cruikshank, D. P., Brown, R. H., Hoefen, T. M., Stephan, K., Moore, J. M., Buratti, B. J., Baines, K. H., Nicholson, P. D., Nelson, R. M. (2008). Compositional mapping of Saturn's satellite Dione with Cassini VIMS and implications of dark material in the Saturn system, *Icarus*, 193, 372-386.

Clark, R. N., Cruikshank, D. P., Jaumann, R., Brown, R. H., Stephan, K., Dalle Ore, C. M. K., Livo, E., Pearson, N., Curchin, J. M., Hoefen, T. M., Buratti, B. J., Filacchione, G., Baines, K. H., Nicholson, P. D., (2012). The Composition of Iapetus: Mapping Results from Cassini VIMS, *Icarus*, 218, 831-860.

Domingue, D. L., Denevi, B. W., Murchie, S. L., Hash, C. D. (2016). Application of multiple photometric models to disk-resolved measurements of Mercury's surface: Insights into Mercury's regolith characteristics. *Icarus*, 268, 172-203.

Filacchione, G. and Capaccioni, F. and McCord, T. B. and Coradini, A. and Cerroni, P. and Bellucci, G. and Tosi, F. and D'Aversa, E. and Formisano, V. and Brown, R. H. and Baines, K. H. and Bibring, J. P. and Buratti, B. J. and Clark, R. N. and Combes, M. and Cruikshank, D. P. and Drossart, P. and Jaumann, R. and Langevin, Y. and Matson, D. L. and Mennella, V. and Nelson, R. M. and Nicholson, P. D. and Sicardy, B. and Sotin, C. and Hansen, G. and Hibbitts, K. and Showalter, M. and Newman, S. (2007). Saturn's icy satellites investigated by Cassini-VIMS. I. Full-disk properties: 350-5100 nm reflectance spectra and phase curves. *Icarus*, 186, 259-290.

Filacchione, G. and Capaccioni, F. and Clark, R. N. and Cuzzi, J. N. and Cruikshank, D. P. and Coradini, A. and Cerroni, P. and Nicholson, P. D. and McCord, T. B. and Brown, R. H. and Buratti, B. J. and Tosi, F. and Nelson, R. M. and Jaumann, R. and Stephan, K. (2010). Saturn's icy satellites investigated by Cassini-VIMS. II. Results at the end of nominal mission. *Icarus*, 206, 507-523.

Filacchione, G. and Capaccioni, F. and Ciarniello, M. and Clark, R. N. and Cuzzi, J. N. and Nicholson, P. D. and Cruikshank, D. P. and Hedman, M. M. and Buratti, B. J. and

Lunine, J. I. and Soderblom, L. A. and Tosi, F. and Cerroni, P. and Brown, R. H. and McCord, T. B. and Jaumann, R. and Stephan, K. and Baines, K. H. and Flamini, E. (2012). Saturn's icy satellites and rings investigated by Cassini-VIMS: III - Radial compositional variability. *Icarus*, 220, 1064-1096.

Filacchione, G., Capaccioni, F., Clark, R. N., Nicholson, P. D., Cruikshank, D. P., Cuzzi, J. N., Lunine, J. I., Brown, R. H., Cerroni, P., Tosi, F., Ciarniello, M., Buratti, B. J., Hedman, M. M., Flamini, E., (2013). The Radial Distribution of Water Ice and Chromophores across Saturn's System, *The Astrophysical Journal*, 766, Issue 2, article id. 76, 5 pp.

Filacchione, G., D'Aversa, E., Capaccioni, F., Clark, R. N., Cruikshank, D. P. Ciarniello, M., Cerroni, P., Bellucci, G., Brown, R. H., Buratti, B. J., Nicholson, P. D., Jaumann, R., McCord, T. B., Sotin, C., Stephan, K., Dalle Ore, C. M. (2016a). Saturn's icy satellites investigated by Cassini-VIMS. IV. Daytime temperature maps, *Icarus*, 271, 292-313.

Filacchione, G. and Capaccioni, F. and Ciarniello, M. and Raponi, A. and Tosi, F. and De Sanctis, M. C. and Erard, S. and Morvan, D. B. and Leyrat, C. and Arnold, G. and Schmitt, B. and Quirico, E. and Piccioni, G. and Migliorini, A. and Capria, M. T. and Palomba, E. and Cerroni, P. and Longobardo, A. and Barucci, A. and Fornasier, S. and Carlson, R. W. and Jaumann, R. and Stephan, K. and Moroz, L. V. and Kappel, D. and Rousseau, B. and Fonti, S. and Mancarella, F. and Despan, D. and Faure, M. (2016b). The global surface composition of 67P/CG nucleus by Rosetta/VIRTIS. (I) Prelanding mission phase. *Icarus*, 274, 334-349.

Hapke, B. (1993). Theory of Reflectance and Emittance Spectroscopy. Topics in Remote Sensing, Cambridge University Press, c1993, Cambridge, UK.

Hapke, B. (2002). Bidirectional reflectance spectroscopy. 5. The coherent backscatter opposition effect and anisotropic scattering. *Icarus*, 157, 523-534.

Hicks, M. D., Buratti, B. J., Nettles, J., Staid, M., Sunshine, J., Pieters, C. M., Besse, S., Boardman, J. (2011). A photometric function for analysis of lunar images in the visual and infrared based on Moon Mineralogy Mapper observations *J. Geophys. Res. (Planets)*, 116, 10.

Hillier, J. K., Buratti, B. J., Hill, K. (1999). Multispectral photometry of the Moon and absolute calibration of the Clementine UV/VIS camera. *Icarus*, 141, 205-225.

Kaidash, V. G., Gerasimenko, S. Y., Shkuratov, Y. G., Opanasenko, N. V., Velikodskii, Y. I., Korokhin, V. V (2009). Photometric Function Variations Observed on the Near Side of the Moon: Mapping. *Solar System Research*, 43, 89-99.

Longobardo, A., Palomba, E., Ciarniello, M., Tosi, F., De Sanctis, M. C., Capaccioni, F., Zambon, F., Ammannito, E., Filacchione, G., Raymond, C. A. (2016). Disk-resolved photometry of Vesta and Lutetia and comparison with other asteroids. *Icarus*, 267, 204-216.

McEwen, A., (1991). Photometric functions for photoclinometry and other applications. *Icarus*, 92, 298-311.

Minnaert, M. (1941). The reciprocity principle in lunar photometry, *Astrophys. J.*, 93, 403-410.

Schenk, P. and Hamilton, D. P. and Johnson, R. E. and McKinnon, W. B. and Paranicas, C. and Schmidt, J. and Showalter, M. R., (2011). Plasma, plumes and rings: Saturn system dynamics as recorded in global color patterns on its midsize icy satellites. *Icarus*, 211, 740-757.

Scipioni, F., Tosi, F., Stephan, K., Filacchione, G., Ciarniello, M., Capaccioni, F., Cerroni, P. (2013). Spectroscopic classification of icy satellites of Saturn I: Identification of terrain units on Dione. *Icarus*, 226, 1331-1349.

Scipioni, F., Schenk, P., Tosi, F., D'Aversa, E., Clark, R., Cruikshank, D. P., Combe, J.-Ph., Dalle Ore, C. (2017). Spectral analysis of Enceladus, Dione, and Rhea surfaces: water ice and sub-micron particles distribution. *Lunar and Planetary Science Conference*, Abstract 1284.

Stephan, K., Jaumann, R., Wagner, R., Clark, R. N., Cruikshank, D. P., Hibbitts, C. A., Roatsch, T. Hoffmann, H. Brown, R. H., Filacchione, G. Buratti, B. J., Hansen, G. B., McCord, T. B., Nicholson, P. D., Baines, K. H. (2010). Dione's spectral and geological properties. *Icarus*, 210, 631-652.

Shkuratov, Y., Starukhina, L., Hoffmann, H., Arnold, G. (1999). A model of spectral albedo of particulate surfaces: Implications for optical properties of the Moon. *Icarus*, 137, 235-246.

Shkuratov, Y. and Kaydash, V. and Korokhin, V. and Velikodsky, Y. and Opanasenko, N. and Videen, G. (2011). Optical measurements of the Moon as a tool to study its surface. *Planetary Space Sciences*, 59, 1326-1371.

Yuhas, R.H., Goetz, A.F.H., Boardman, J.W., (1992). Discrimination among semi-arid landscape endmembers using the spectral angle mapper (SAM) algorithm. In: *Summaries of the 4th JPL Airborne Earth Science Workshop*, JPL Publication 92- 41, 147-149.

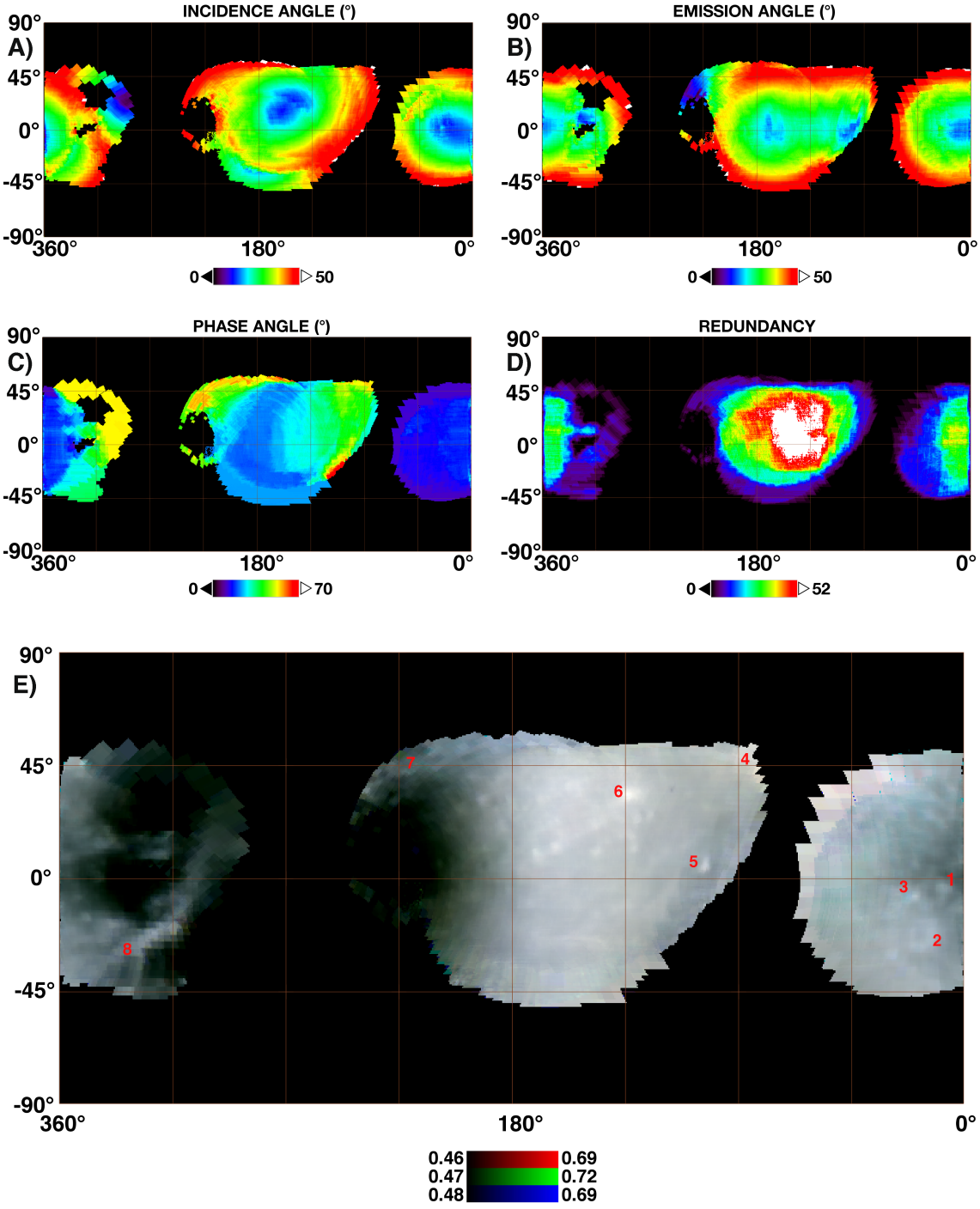

Figure 2. Average geometry parameters for visible albedo map shown in cylindrical projection. Panel A): incidence angle. Panel B): emission angle. Panel C): phase angle. Panel D): VIMS data redundancy. Panel E): Dione visible color albedo map at B=0.44 μm, G=0.55 μm and R=0.7 μm. Numerals indicate the position of the geological features resolved on the map: 1) Antenor crater; 2) Dido crater; 3) Romulus crater; 4) Creusa crater ejecta; 5) Sagaris crater; 6) Aeneas crater; 7) Padua Chasmata; 8) Eurotas Chasmata.

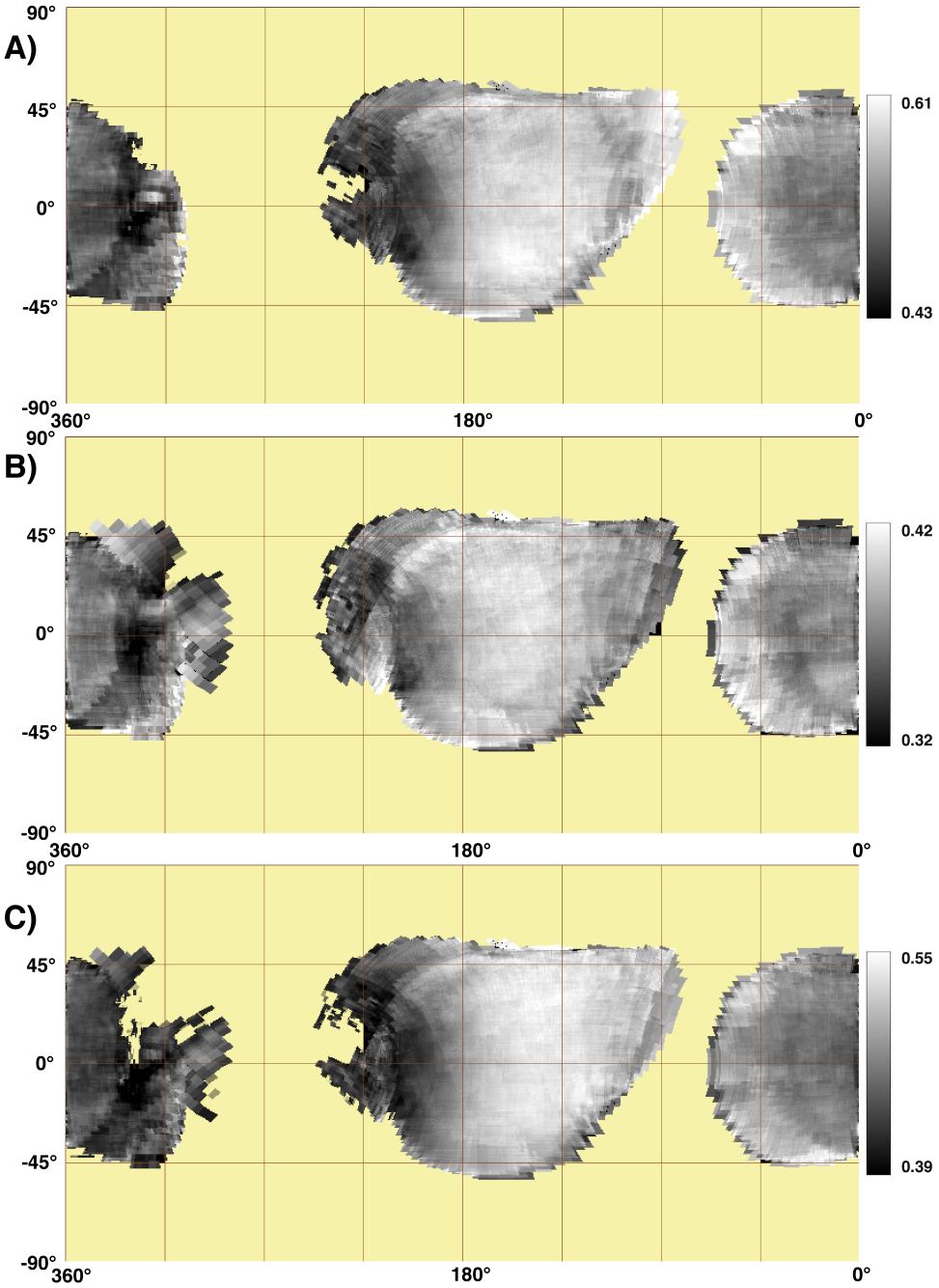

Figure 3. Dione infrared albedo maps at 1.046 μm (panel A), 1.540 μm (panel B) and 2.200 μm (panel C).

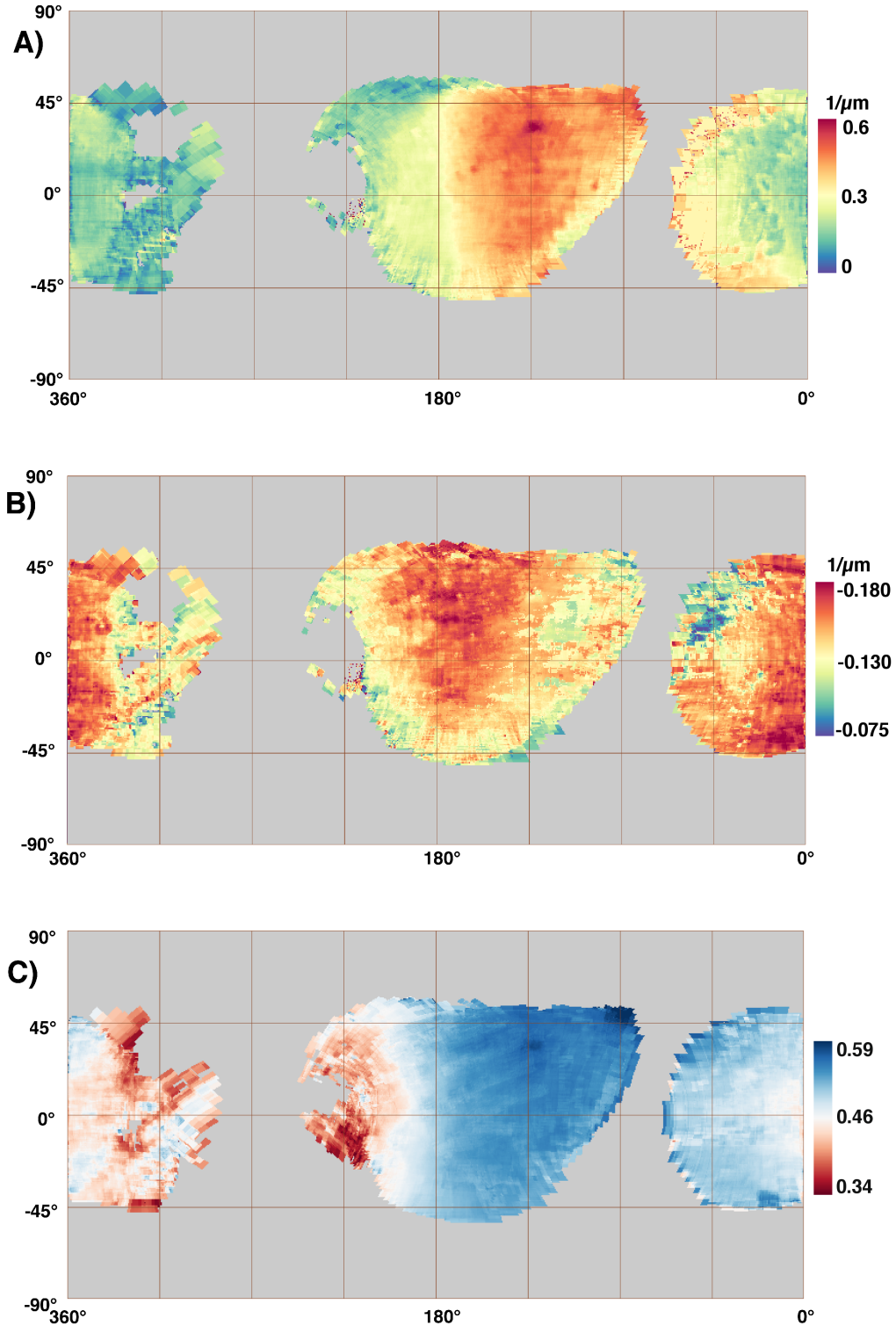

Figure 4. Dione cylindrical maps for 0.35-0.55 μm slope (panel A), 0.55-0.95 μm slope (panel B) and 2.050 μm water ice band depth (panel C).